

Spinodal superlattices of topological insulators

Demet Usanmaz,¹ Pinku Nath,¹ Cormac Toher,¹ Jose Javier Plata,¹

Rico Friedrich,¹ Marco Fornari,² Marco Buongiorno Nardelli,³ and Stefano Curtarolo^{4,5,*}

¹*Department of Mech. Engineering and Materials Science, Duke University, Durham, NC 27708, USA.*

²*Department of Physics, Central Michigan University, Mount Pleasant, MI 48859, USA.*

³*Department of Physics, University of North Texas, Denton, TX 76203, USA.*

⁴*Materials Science, Electrical Engineering, Physics and Chemistry, Duke University, Durham, NC 27708, USA.*

⁵*Fritz-Haber-Institut der Max-Planck-Gesellschaft, 14195 Berlin-Dahlem, Germany.*

(Dated: September 6, 2018)

Spinodal decomposition is proposed for stabilizing self-assembled interfaces between topological insulators (TIs) by combining layers of iso-structural and iso-valent TlBiX_2 ($X=\text{S, Se, Te}$) materials. The composition range for gapless states is addressed concurrently to the study of thermodynamically driven boundaries. By tailoring composition, the $\text{TlBiS}_2\text{-TlBiTe}_2$ system might produce both spinodal superlattices and two dimensional eutectic microstructures, either concurrently or separately. The dimensions and topological nature of the metallic channels are determined by following the spatial distribution of the charge density and the spin-texture. The results validate the proof of concept for obtaining *spontaneously forming* two-dimensional TI-conducting channels embedded into three-dimensional insulating environments without any vacuum interfaces. Since spinodal decomposition is a controllable kinetic phenomenon, its leverage could become the long-sought enabler for effective TI technological deployment.

INTRODUCTION

Modern materials technology has been efficiently used to reduce the size and increase the functionality of electronic devices and electrical machinery. Semiconductors find a place in a wide range of applications, such as transistors,¹ detectors,^{2,3} light emitting diodes,⁴ and lasers,⁵ while powerful permanent magnets are used in renewable power generation and electric motors central to the post fossil fuel economy.⁶ Many of these technologies require scarce elements to achieve exotic properties, such as the reliance of transparent conductors on indium,⁷ or the dependence of permanent magnets on rare earth elements, *e.g.* dysprosium.^{8,9} Similar properties can be replicated by fabrication of heterostructures, where the distinct band structures of the constituent materials facilitates the engineering of electronic properties inside device components. However, this technology relies on artificial growth methods, which increase both the time and cost of fabrication. Exploring alternative synthesis methods and materials is important for overcoming this challenge.¹⁰

Here, we propose a new approach by combining advanced thermodynamic and electronic structure concepts for novel materials design. The design and manufacture of embedded 2D metallic channels in a 3D insulating matrix will enhance the functionality of scalable circuitry for high-performance electronics. Our approach to obtain these channels exploits easy-to-make self-organizing thermodynamically driven morphologic microstructures. This is an alternative to current efforts, where fabrication of heterostructures has relied mostly on artificial growth methods, very likely with thermodynamically unstable or metastable phases.¹¹⁻¹³ Topological insulators (TIs), which exhibit insulating behavior in bulk and metallic states at their boundaries, are the most promising materials for this purpose.¹⁴⁻¹⁸ The presence of metallic states relies on the spin-orbit induced band inversion in bulk materials, protected by either time-reversal or crys-

tal symmetry.^{17,19-22} The characteristics of the gapless boundary states are linear dispersion in the bulk band gap, spin-texture, robustness against scattering by non-magnetic impurities, and symmetry protection. Studies have demonstrated that the formation of heterostructures,²³⁻²⁶ alloying,^{20,27} and thickness engineering²⁸ have advantages for controlling the electronic properties of TIs. In addition, recent studies show that it is possible to observe novel properties in TI superlattices, such as both time-reversal and crystal symmetry protected surface states,^{29,30} band structure tuning through a topological phase transition,³¹ topologically nontrivial surface states in a magnetic-TI/TI superlattice,³² and the realization of 3D Weyl semimetal phases.³³ To fully exploit TIs in future devices, a detailed exploration of TI heterostructures/superlattices is needed.

The natural formation of interfaces based on thermodynamic stability is interesting: recent studies have proposed the use of spinodal decomposition to generate materials with *ad hoc* characteristics which enhance the properties of thermoelectric materials.³⁴⁻³⁷ Spinodal decomposition is a phase separation mechanism, where below the critical temperature T_c , the components separate into distinct homogeneous regions with different physical and chemical properties.³⁸⁻⁴⁰ This allows TI heterostructures consisting of layers of thermodynamically stable phases to be constructed, which is the key to durable and long-lasting applications. Moreover, creating boundaries between chemically distinct but iso-structural phases of some insulating materials has already led to remarkable properties.⁴¹⁻⁴³

The candidate materials, (Tl, Bi)-based ternary chalcogenides, TlBiX_2 ($X=\text{S, Se, Te}$), are a rare group in which TIs and trivial-insulators share the same crystal structure. TlBiSe_2 and TlBiTe_2 are 3D TI materials while TlBiS_2 is a trivial insulator. These properties allow the investigation of the TI/TI and trivial-insulator/TI boundaries between phases that are both iso-structural (important for forming commensurate interfaces) and iso-

valent. Furthermore, TlBiSe₂ is a TI similar to Bi₂Se₃ with the advantage of having an almost perfect Dirac cone at the Γ -point, which is separated from the bulk states and thus allows for the investigation of the transport properties of the TlBiSe₂ boundary states independently of the bulk states.^{44–46} The topologically trivial system, TlBiS₂, has a clear band gap at the surface. Gapless metallic states arise at the onset of the topological phase transition, occurring under strain and/or an external electric field.^{47–49} Another interesting characteristic of this group of materials is the topological phase transition from trivial-insulator to TI resulting from substituting S with Se atoms in TlBi(S_{1-x}Se_x)₂.²⁷ This tunes the lattice constant and spin-orbit coupling (SOC), so that a topological phase transition takes place at the critical point ($x_c \sim 0.48$) and a 3D-Dirac point arises. For ($x_c \leq x \leq 1$), gapless surface states appear in the electronic band gap.²⁷ In contrast, other independent studies report that the TlBi(S_{1-x}Se_x)₂ system has gapped surface states for $0.6 \leq x \leq 0.9$,^{50,51} despite being in the topologically non-trivial phase. The physical cause of the opening of the gap is not known, although it is possible that the answer lies in the thermodynamic properties. Additionally, Weyl semimetal phases are predicted for TlBi(S_{1-x}Se_x)₂ and TlBi(S_{1-x}Te_x)₂ alloys at $x = 0.5$ in the case of layer-by-layer growth (Tl-Se(Te)-Bi-S) for certain critical values of the c/a ratio.⁵² Other interesting phenomena, specifically Rashba spin-splitting and the topological proximity effect, have been observed on the Bi(1 bilayer)/TlBiS₂ and Bi(1 bilayer)/TlBiSe₂ surfaces, respectively.¹³ These interesting properties make this group of materials promising candidates for superlattice studies.

In this work, we combine thermodynamic and electronic structure analysis to define a natural design strategy for TI superlattices that can be an alternative to the very costly and time-consuming experimental artificial growth methods. The current study is built on the following aspects: **i.** Identify the miscibility gap of each pair of TlBiX₂ ($X=S, Se, Te$) compounds by calculating the thermodynamic phase diagram and predicting the consolute temperature (T_c). **ii.** Design boundaries between constituent materials to predict appropriate ranges of composition guaranteeing the topologically protected gapless metallic states. **iii.** Track the spatial distribution of the charge density of these boundaries to verify the existence of topologically protected 2D metallic channels in the 3D insulating matrix.

METHODS

Thermodynamics. The enumeration of configurations, determination of ground state structures, and prediction of energies of more structures through Cluster Expansion are performed within the ATAT framework.^{53–55} The temperature-composition phase boundaries are obtained with Monte Carlo simulations.⁵³ From this data, using the definition of the Gibbs free energy in Ref.,¹⁰ proper

derivatives are calculated to determine the binodal and spinodal *loci*.

Bulk. Bulk structures are fully relaxed using the AFLOW high-throughput framework^{56–68} and the DFT Vienna *Ab-initio* Simulation Package (VASP).⁶⁹ Geometry optimizations are performed following the AFLOW standard,⁵⁸ using PAW pseudopotentials⁷⁰ and the PBE parametrization of the GGA exchange and correlation functional.⁷¹ A high energy-cutoff (40% larger than the maximum cutoff of all pseudopotentials) is used for all calculations. Reciprocal space integration is performed using a mesh of 8000 \mathbf{k} -points per reciprocal atom. Structures are fully relaxed (cell volume and ionic positions) until the energy difference between two consecutive ionic steps is smaller than 10^{-4} eV. Electronic structure calculations for TlBiS₂, TlBiSe₂, and TlBiTe₂ are performed with SOC.

Interfaces. The lattice parameters (stress) and ionic positions (forces) are optimized until all force components on each ion are less than 0.001 eV/Å. The outer s and p electrons are treated as valence electrons with the rest included in the core. A kinetic energy cutoff of 392 eV and a Γ -centered $9 \times 9 \times 1$ \mathbf{k} -point mesh is used. Electronic structure calculations are performed with SOC.

RESULTS AND DISCUSSION

TABLE 1. Cross-validation (CV) score (in meV), consolute temperatures (T_c) (in K), and critical compositions (x_c) of TlBiS₂-TlBiSe₂, TlBiSe₂-TlBiTe₂, and TlBiS₂-TlBiTe₂.

	TlBiS ₂ -TlBiSe ₂	TlBiSe ₂ -TlBiTe ₂	TlBiS ₂ -TlBiTe ₂
CV score	0.63	1.15	4.30
T_c	162	400	1040
x_c	0.4	0.4	0.35

Thermodynamic properties. Figure 1(a, b, c) illustrates the calculated and predicted formation enthalpies (ΔH_f) from DFT and cluster expansion, respectively. All three systems have positive ΔH_f for the entire range of compositions ($0 < x < 1$): these systems are immiscible at 0K. Cluster expansion predictions well agree with DFT calculated energies with small cross validation scores which are tabulated in Table 1. The miscibility of two isomorphous systems can be addressed using the classic Hume-Rothery rules⁷⁴ based on four properties: atomic radius, crystal lattice, valence, and electronegativity. These three systems have the same crystal structure; S, Se, and Te atoms are from the same group in the periodic table and have similar electronegativities; while the atomic radii range from 1.04 Å for S, to 1.17 Å for Se, and 1.37 Å for Te. This difference creates a mismatch between the constituent lattices, reducing interface coherence, eventually leading to phase decomposition.

Combining the output of the Monte Carlo simulations with a previously developed model¹⁰ enables the inexpensive and efficient prediction of the spinodal curve, a quantity which is not usually calculated. The calculated phase

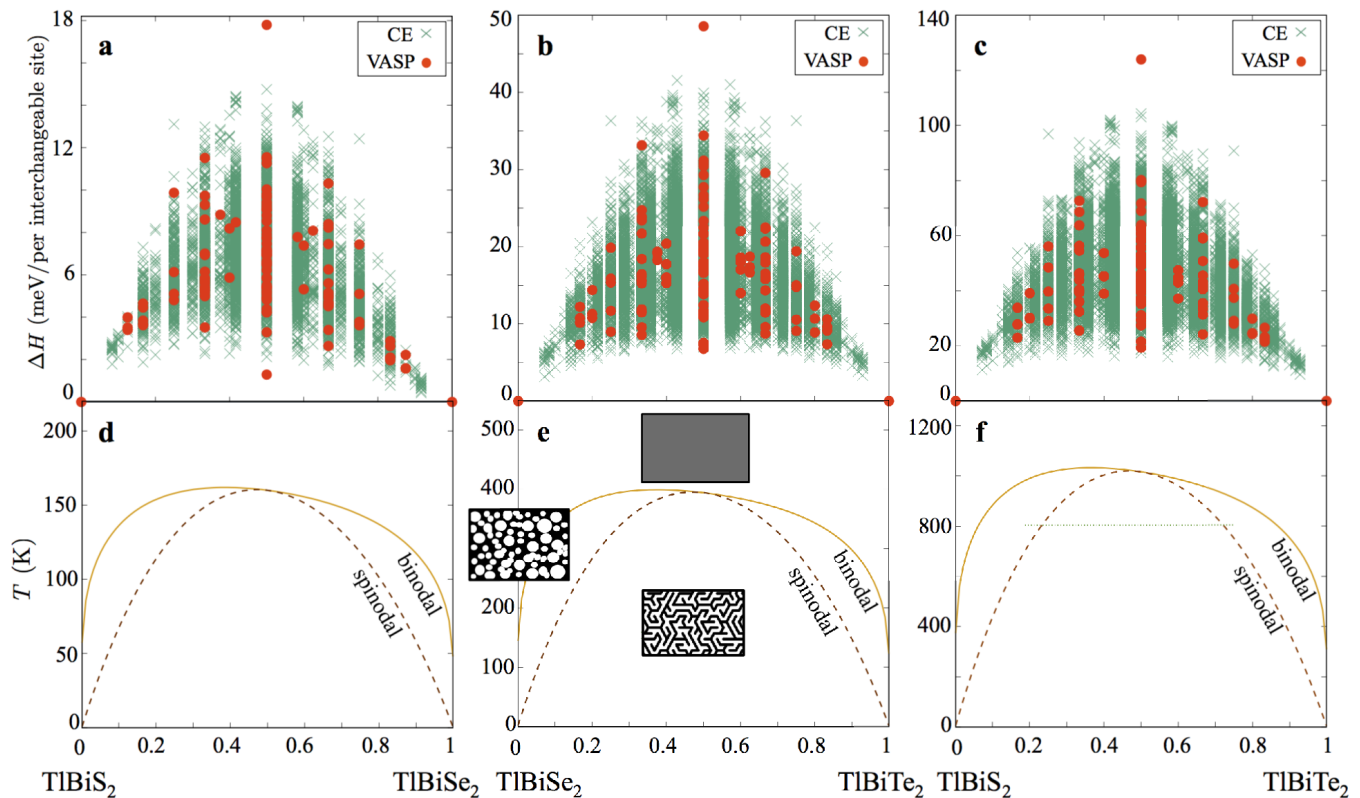


FIG. 1. Formation enthalpies of the (a) TlBiS₂-TlBiSe₂ (b) TlBiSe₂-TlBiTe₂ (c) TlBiS₂-TlBiTe₂ structures using DFT calculations (●) and cluster expansion technique (×) (upper panel). Their respective binodal (—) and spinodal curves (---) are illustrated in the lower panels (d,e,f). The eutectic isotherm, from Ref.^{72,73} is illustrated with (· · ·).

diagrams in Figure 1(d,e,f) show that TlBiS₂-TlBiSe₂, TlBiSe₂-TlBiTe₂, and TlBiS₂-TlBiTe₂ systems have an asymmetric miscibility gap. The asymmetric behavior of the miscibility gap is typical when the substitution atoms of the two end members have very different atomic radii.⁷⁵

The calculations indicate that TlBiS₂ and TlBiSe₂ are miscible above 162K (Figure 1(d)). To the best of our knowledge, for the TlBiS₂-TlBiSe₂ system, there are no experimentally obtained phase diagram data available below 930K, at which temperature both compounds are still completely miscible.⁷³ Successful high temperature synthesis followed by cooling to room temperature has been reported for several compositions.^{27,50,51} For these experiments, homogeneity for $x=0.8$ is indicated at the 8 μm scale by electron probe microanalysis, although it is unclear at which temperature the analysis was performed.⁵⁰ Angle-resolved photoemission spectroscopy (ARPES) measurements to investigate the novel electronic properties are performed at very low temperatures, where no thermodynamic data is available. The calculated phase diagram (Figure 1(d)) indicates that TlBiS₂ and TlBiSe₂ should start to spinodally decompose when the system is cooled down for ARPES measurements. However, due to slow kinetics at low temperatures, the sample may not have sufficient time to complete the decomposition process prior to the electronic structure measurements. Without reaching equilibrium, different time-temperature profiles

will lead to different experimental results. Therefore, depending on the details of the experimental procedure, the samples that the ARPES measurements are performed on could be at different stages of phase separation, which would explain the different results obtained in the two independent electronic structure studies.^{27,50}

For TlBiSe₂-TlBiTe₂ there are no experimental data available below 760K.⁷³ The Monte Carlo simulations show that TlBiSe₂ and TlBiTe₂ become immiscible below 400K (Figure 1(e)). This system is suitable for the practical realization of self-organized heterostructures: It is possible to obtain a homogeneous stable phase around 500K (well below the melting point of the materials); and to obtain self-organized heterostructures between chemically distinct but iso-structural phases at room temperature.

The predicted results show that the TlBiS₂-TlBiTe₂ system is immiscible below 1040K. Reported experimental results indicate a eutectic isotherm at $T_e \sim 810\text{K}$.^{72,73} Its range of composition is depicted in Figure 1 as a horizontal line. There are two scenarios. **i.** Any mixture starting outside the eutectic *solvi* range [TlBi(S₂-rich,Te₂-poor) or TlBi(S₂-poor,Te₂-rich)] and solidifying through the miscibility gap will not undergo eutectic transformation and eventually will find the spinodal line at lower temperature. **ii.** Any composition within the eutectic range will allow a fraction of the liquid to reach $x_e \sim 64\%$

causing a eutectic transformation. This is an interesting regime: the potentially sudden atomic reorganization, the release of latent heat, and the concomitant entrance in the spinodal region, will promote the formation of interesting phase-separating 2D microstructures which can be further tailored through heat treatment (eutectic superlattices). Such organizations could have surprising electronic properties. Experiments at and around the eutectic composition with different time-temperature profiles are highly suggested. Compositions slightly above the minimum and slightly below the maximum eutectic range could also lead to interesting properties.

Since excess vibrational free energy is neglected in our calculations, lower T_c values can be expected in experiment, and similar behavior is reported for other systems.^{75,76} Also, as a result of the slow kinetics at low temperatures, experimental proof of the miscibility gap has not been reported yet for these systems.

The calculations show that larger mismatches between the size of the interchangeable atoms corresponds to higher T_c values for these three systems. Similar behavior has been observed for various systems, such as refractory carbide solid solutions,⁷⁶ lead chalcogenides¹⁰ and some carbonate quasi-binary systems.⁷⁷

Boundaries of immiscible systems. Boundaries of immiscible systems are modelled by keeping the phase boundary wavelength, λ_{\max} , constant. Generally, λ_{\max} ranges from 10 to 100 nm for various systems.^{36,78,79} For these calculations, λ_{\max} is set to 13-14 nm for computational feasibility. This value also provides sufficient thickness for investigating gapless metallic states.^{52,80}

In the crystalline solution, finite thickness regions form and interfaces emerge in between them. Biaxial strain of opposite sign is imposed on both sides of the interface until they reach the mutual lattice parameter. Therefore, the strain is shared between each side of the interface (one compressive and the other tensile) so that the misfit between the lattices is reduced. For small strains, the system remains coherent. However, in the case of large strain, the system interfaces can become semi-coherent with periodically repeating misfit dislocations. In epitaxially grown semiconductor heterostructures, the misfit can be accommodated by uniform elastic strain for films below a critical thickness.^{81,82} Analogously, we propose that coherent interfaces can be obtained in the spinodally decomposed systems, even for big lattice misfits, by keeping one region thinner than the critical thickness. Therefore, the investigation of the large lattice mismatch systems $\text{TlBiSe}_2/\text{TlBiTe}_2$ and $\text{TlBiS}_2/\text{TlBiTe}_2$ is performed by focusing around the end compositions where one region is very thin. For the moderate lattice mismatch system $\text{TlBiS}_2/\text{TlBiSe}_2$, the whole compositional range is investigated.

If the band inversion takes place at Γ in 3D, then the Dirac points will always appear at Γ in 2D, independent of the lattice direction.¹⁸ Therefore, the superlattices

are modelled along the (111) direction of the rhombohedral cell for computational feasibility, while still capturing the relevant physics. Creating boundaries between iso-structural and iso-valent phases eliminates the effect of dangling bonds on the electronic structure due to the continuous nature of the system. For these calculations, the boundaries are placed between the weakly bonded interfacial X -Tl layers, although these layers are still considered as strongly interacting due to their ionic/covalent bonding. This is in contrast to Bi_2Se_3 and Bi_2Te_3 , which have weak van der Waals bonds between quintuple layers.

The superlattices are modelled by considering the 0K configurations, since the sample cleaving and the ARPES measurements are mostly carried out at low temperatures (~ 15 -30K).^{27,83} At 0K, only two separate phases can exist; an interface forms between TlBiS_2 and TlBiSe_2 , TlBiSe_2 and TlBiTe_2 , or TlBiS_2 and TlBiTe_2 .

The band alignment needs to be investigated to define the position of the gapless metallic states and to understand the interaction between the constituent materials bands. First, the average electrostatic potential difference between the two constituent materials is obtained. Next, the difference between the valence band edge and the average electrostatic potential of each constituent material (which is under the same biaxial strain as in the superlattice) is calculated. For each system, the band alignment is investigated for two compositions. The results show that although the band offset magnitude changes, the band alignment character of the system is preserved. This demonstrates the feasibility of engineering the bands of spinodally decomposed materials through compositional tuning.

$(\text{TlBiS}_2)_{1-x}(\text{TlBiSe}_2)_x$ boundaries. These boundaries represent a possible trivial-insulator/TI system. In order to find the composition(s) where 2D-gapless metallic states arise, a wide range of composition space is scanned (Figure 2(a)) while adhering to a constant value of λ_{\max} .

The position of the interface states are illustrated by projecting the contribution of four atomic layers from each side of the boundaries. As can be seen in Figure 2, metallic states emerge for the $8/18 \leq x \leq 13/18$ compositional range and the system has a tiny band gap (Figure 2(d-i)), which is smaller than the room temperature thermal energy (0.025 eV), and is within the DFT error range. The atom resolved band structures indicate that the lower branch of the metallic state originates from TlBiSe_2 and the upper branch is from TlBiS_2 . The system has staggered (type-II) band alignment (Figure 2(b)), where the TlBiS_2 conduction band and the upper branch of the TlBiSe_2 Dirac cone fall in the same energy range. In fact, the upper branch of the Dirac cone is embedded in the TlBiS_2 conduction bands and the biggest contribution comes from TlBiSe_2 at $\bar{\Gamma}$.

Analyzing the projected charge density of the metallic states can provide a better spatial understanding of the electronic structure of the system. This projection is presented in Figure 2(c) for composition $x = 11/18$ at

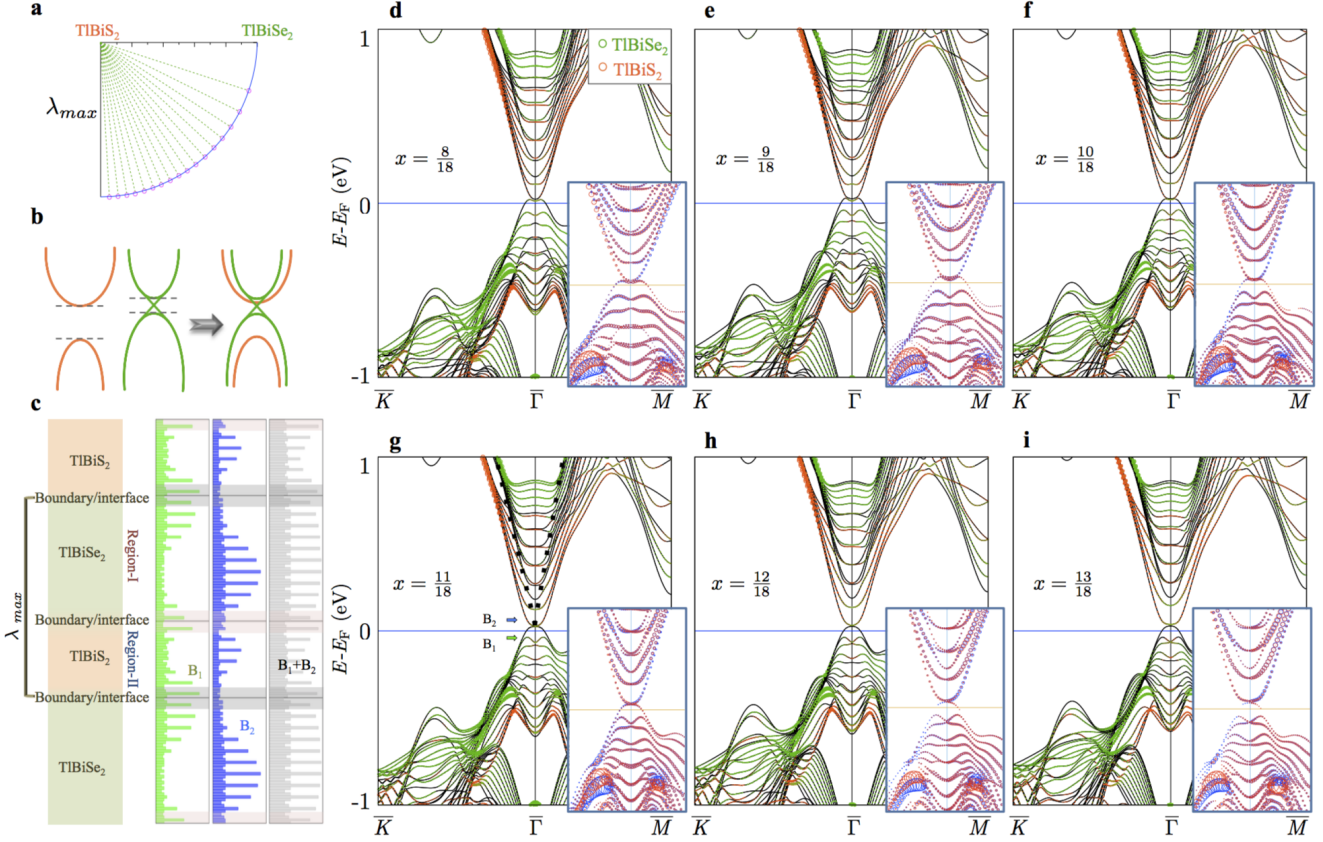


FIG. 2. (a) Schematic representation of considered compositions and (b) band alignment for $(\text{TlBiS}_2)_{1-x}(\text{TlBiSe}_2)_x$. (c) Spatial distribution of the charge density of states B_1 and B_2 at $\bar{\Gamma}$ for $x = 11/18$. The summed charge density of both states is also shown, and exhibits a symmetric shape over the whole system. Electronic band structure of $(\text{TlBiS}_2)_{1-x}(\text{TlBiSe}_2)_x$ boundaries with projection of four atomic layers from each side of the boundaries for compositions (d) $x = 8/18$, (e) $x = 9/18$, (f) $x = 10/18$, (g) $x = 11/18$, (h) $x = 12/18$ and (i) $x = 13/18$. The insets show the band structure with in-plane spin contributions. The size of symbols are proportional to the degree of in-plane spin polarization in the five atomic layers nearest the interface, and the red and blue colors correspond to the in-plane spin-up and spin-down directions, respectively. $\bar{K} - \bar{\Gamma} - \bar{M}$ represents the path in the two-dimensional Brillouin zone of the rhombohedral lattice.

$\bar{\Gamma}$. B_1 and B_2 represent the highest and lowest points of the bands which form the Dirac point at $\bar{\Gamma}$. For B_1 , the charge density accumulates around the interfaces with some penetration through the interior layers. This agrees well with the reported studies which indicate that the charge density of the surface states decays much slower for TlBiX_2 , specifically for TlBiSe_2 , than for Bi_2Se_3 and Bi_2Te_3 .^{80,84,85} For the B_2 state, the charge density shifts away from the interface as a result of the interaction between the TlBiSe_2 Dirac cone and the TlBiS_2 conduction band minimum. This is consistent with previous studies of TI heterostructures, which show that depending on the interaction strength at the interface, the spatial position of the Dirac states can shift away from the interface.^{25,86,87} The orbital character of the B_1 and B_2 bands at $\bar{\Gamma}$ are mainly p_z , consistent with surface states of TlBiSe_2 , and different from the p_{xy} orbital character of the valence band maximum and conduction band minimum of the bulk (see Supplementary Information). Due to the spatial shift of the B_2 state, the total charge density at the Dirac-like point is distributed all over

the material instead of accumulating at the interfaces (Figure 2(c)). It can, however, be expected that for larger superlattices with thicker TlBiX_2 regions (larger λ_{max}), the states will be localized close to the interface. The spin polarized band structure (Figure 2(d-i), insets) illustrates that spin degeneracy is lifted for the upper branch of the gapless metallic states, which is from the trivial insulator (TlBiS_2), specifically for $x=10/18$ and $11/18$. This behavior is similar to the recent studies which report that in semiconductor/TI heterostructures, semiconductor states can acquire a nontrivial spin texture as a result of their interaction with the TI interface states.^{88,89}

$(\text{TlBiSe}_2)_{1-x}(\text{TlBiTe}_2)_x$ boundaries. This system contains two 3D TI materials. The presence of gapless topological interface states at the junction of two TIs depends on the helicity and magnitude of the Fermi velocity of the TI surface states, and on the mirror symmetry of the system.^{90,91} Due to the focus around the end compositions at the $\text{TlBiSe}_2(\text{TlBiTe}_2)$ -rich part, the $\text{TlBiTe}_2(\text{TlBiSe}_2)$ region becomes quite thin, behaving like an ultra thin film.

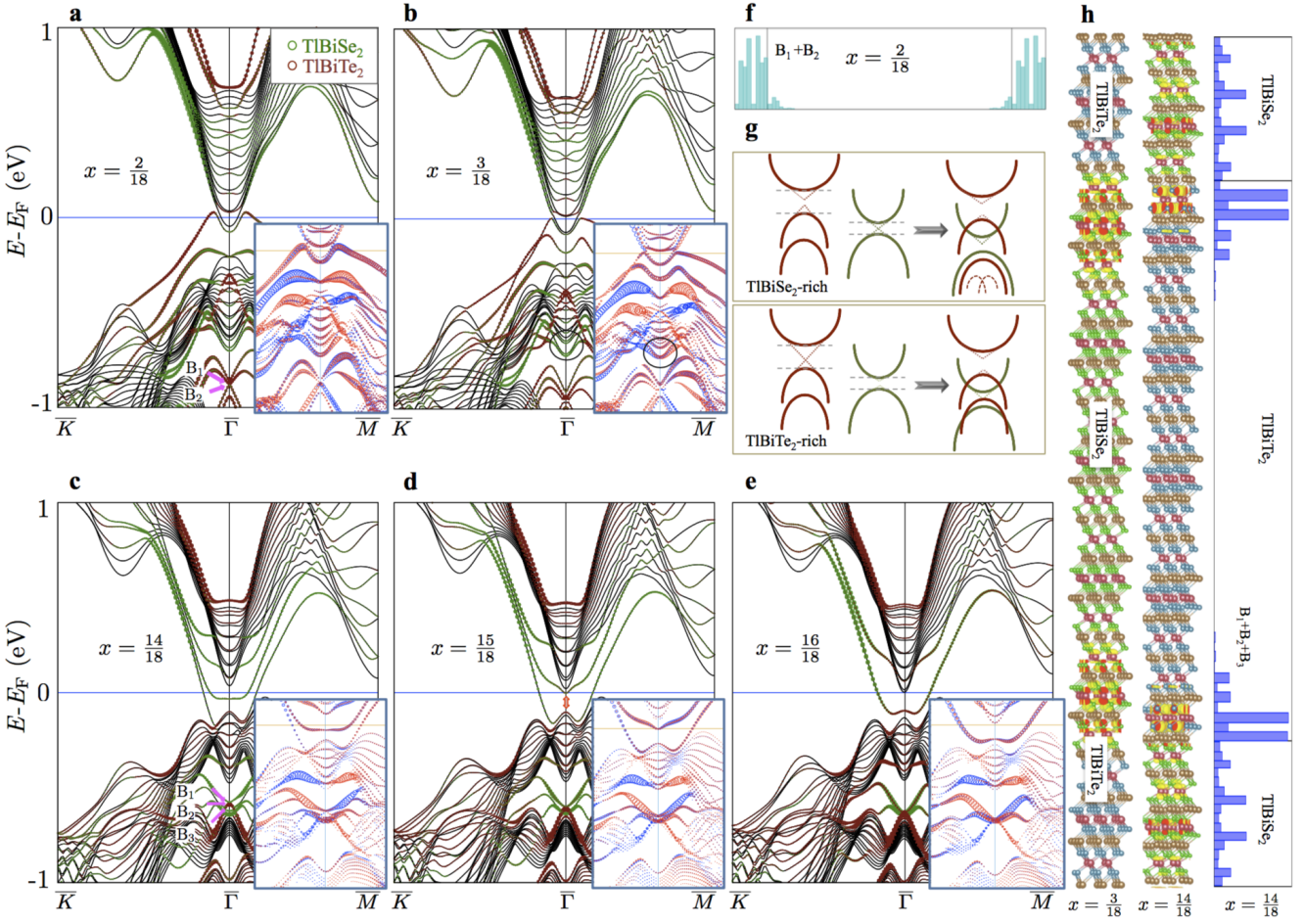


FIG. 3. Electronic band structure of $(\text{TlBiSe}_2)_{1-x}(\text{TlBiTe}_2)_x$ boundaries for compositions (a) $x = 2/18$, (b) $x = 3/18$, (c) $x = 14/18$, (d) $x = 15/18$, and (e) $x = 16/18$. The contribution of four atomic layers from each side of the region, or the contribution of the entire thin region (in the case of very thin regions), are projected onto the electronic band structures. (f) and (h) Projected and isosurface representation of summed charge density for $x = 2/18$, $3/18$, and $14/18$. (g) Schematic representation of band alignment of $(\text{TlBiSe}_2)_{1-x}(\text{TlBiTe}_2)_x$ boundaries for TlBiSe_2 -rich and TlBiTe_2 -rich compositions. The insets show the band structure with in-plane spin contributions. The size of symbols are proportional to the degree of in-plane spin polarization in the five atomic layers nearest the interface, and the red and blue colors correspond to the in-plane spin-up and spin-down directions, respectively (color code: \bullet Bi \bullet Tl \bullet Se \bullet Te).

In addition, the systems have broken band alignment, where the fundamental band gaps of the two constituent materials do not overlap. No interaction is expected between any present TlBiSe_2 and TlBiTe_2 metallic interface states. However, due to the narrow band gap of the systems, the overlap between the electron and hole states of TlBiSe_2 and TlBiTe_2 is large. The contribution of four atomic layers from each side of the region or the contribution of the entire thin region (in the case of very thin regions) are projected onto the electronic band structures. This illustrates how changing the composition affects the interface states.

The TlBiX_2 systems have ionic/covalent bonding rather than van der Waals bonding between the layers. Interlayer separation changes with respect to bulk at the interface between TlBiSe_2 and TlBiTe_2 are less than 0.2 \AA , indicating that the interaction at the interface remains strong. As a result of this strong interaction, reshaping of the bands

is expected. This is different than the simple superposition of bands where interfacial coupling is weak. The band structures for various compositions are presented in Figure 3. It can be clearly seen that around the two end compositions, one region is thick enough to reproduce the bulk band features. Since the system is periodically repeating and the vacuum interface is neglected, the Dirac cone from the surface states does not show up in the electronic band structure. Therefore, in contrast to the TI heterostructures where vacuum interfaces are considered, multiple Dirac cones are not expected here.^{87,89}

For TlBiSe_2 -rich compositions ($x=2/18$ and $3/18$), the TlBiSe_2 region is much wider than TlBiTe_2 , and wider than the theoretically defined critical thickness for the emergence of the Dirac cone. For these compositions the upper branch of the Dirac cone is present near the Fermi level. The lower branch is suppressed by TlBiTe_2 bulk states, and no gapless states are present. At $x = 2/18$,

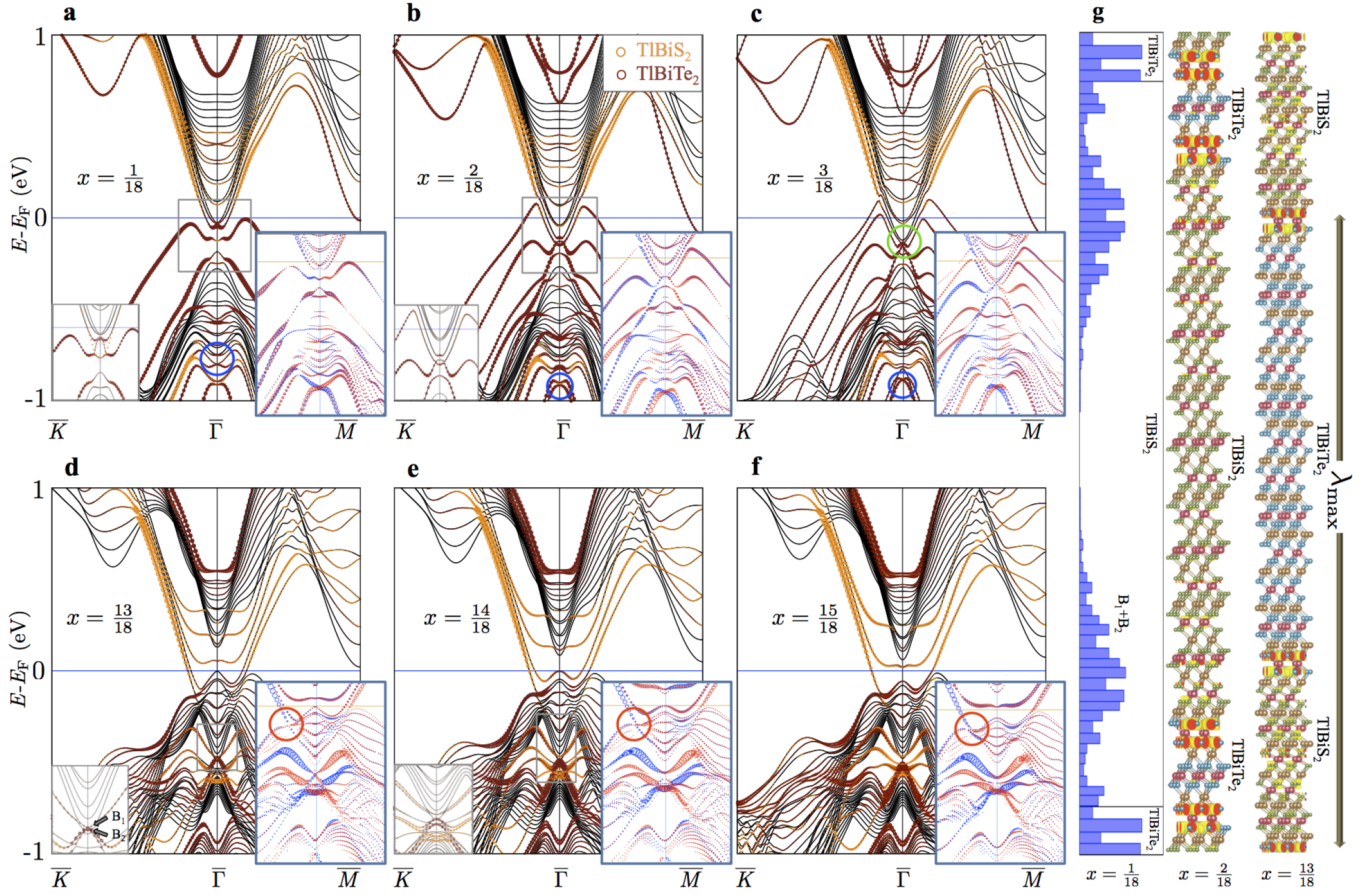


FIG. 4. Electronic band structure of $(\text{TlBiS}_2)_{1-x}(\text{TlBiTe}_2)_x$ boundaries for compositions (a) $x = 1/18$, (b) $x = 2/18$, (c) $x = 3/18$, (d) $x = 13/18$, (e) $x = 14/18$, and (f) $x = 15/18$. The contribution of four atomic layers from each side of the region, or the contribution of the entire thin region (in the case of very thin regions), are projected onto the electronic band structures. (g) Projected and isosurface representation of summed charge density at the Dirac point for $x = 1/18$, $x = 2/18$ and $x = 14/18$. The insets show the band structure with in-plane spin contributions. The size of symbols are proportional to the degree of in-plane spin polarization in the five atomic layers nearest the interface, and the red and blue colors correspond to the in-plane spin-up and spin-down directions, respectively (color code: ●Bi ●Tl ●S ●Te).

X-shaped gapless metallic states emerge around -0.85 eV, and these states are mainly from the TlBiTe_2 region and mostly localized at the interface (Figure 3(f)). However, they are topologically trivial states since they have spin degeneracy. A similar X-shaped band is reported for one bilayer Bi on the TlBiSe_2 surface.¹³ At $x = 3/18$ (Figure 3(b)), gapless interface states arise around -0.7 eV at $\bar{\Gamma}$ (black ellipse). The isosurface charge density indicates that these states are TlBiSe_2 interface states and have p_z character. Also, the spin resolved band structure shows that these bands are spin polarized (Figure 3(b), inset). A similar state is reported for other TI superlattices.^{29,30,92,93}

At the TlBiTe_2 -rich compositions, the thickness and relative strains on the regions change. This does not alter the band alignment character, only tunes the band offset. For these compositions, the TlBiTe_2 region is thick enough to obtain a Dirac cone from interface states, but the interface states are gapped near the Fermi level, as indicated by the red arrow (Figure 3(d)). However,

Dirac-like gapless states emerge between the TlBiSe_2 and TlBiTe_2 states around -0.5 eV. In order to understand the nature of these states, the projected charge density as well as the isosurface charge density at $\bar{\Gamma}$ is presented in Figure 3(h) for $x = 14/18$. The plots indicate that these Dirac-like points are spread across the TlBiTe_2 interface state and the TlBiSe_2 bulk state. These types of bands are reported for TI heterostructures and are described as mixed-character bands.^{87,89} Thusly, instead of two metallic channels, only one metallic channel arises, which includes the entire TlBiSe_2 region. The upper and lower branches of the Dirac-like points have opposite spin polarization (Figure 3(c-e), insets), indicating that they are topologically protected.

$(\text{TlBiS}_2)_{1-x}(\text{TlBiTe}_2)_x$ boundaries. This system is another example of a possible trivial-insulator/TI system with a large lattice misfit.

In the TlBiS_2 -rich compositions, the TlBiTe_2 region is very thin, so the system is a superlattice of a trivial in-

sulator and an ultra thin film of 3D TI with broken band alignment. The band structures in Figure 4(a-c) demonstrate that at compositions $x = 1/18$, $2/18$, and $3/18$, there is band inversion between the TlBiS_2 and TlBiTe_2 states, and their hybridization causes the gap to open near $\bar{\Gamma}$. This indicates the non-trivial nature of the system. In addition, for $x = 1/18$ a Dirac-like point appears around -0.8 eV (blue circle) and the projected charge density (Figure 4(g), left) demonstrates that charges accumulate close to the TlBiS_2 edge, with some shift due to the interaction with the TlBiTe_2 states, along with some contribution from the TlBiTe_2 region. The spin texture indicates that these states are spin polarized (Figure 4(a), inset). Increasing the composition (x) tunes the relative thickness of the TlBiS_2 and TlBiTe_2 regions, as well as the strains on them, changing the population and position of the states. Inverted bands exist around $\bar{\Gamma}$ for the TlBiS_2 -rich compositions. In addition, Rashba-like states emerge around -0.9 eV (Figure 4(b,c)). As can be seen from Figure 4(c), at $x = 3/18$ a Dirac point emerges in the inverted gap near the Fermi level. The spatial distribution of the Dirac point charge density shows that charge accumulates around the interface, mainly at the edge of the TlBiTe_2 region. In contrast to the surface Dirac cones, these states have p_{xy} orbital character. The spin texture of the Dirac cone is presented in Figure 4(c), inset.

At the TlBiTe_2 -rich region, $(\text{TlBiS}_2)_{1-x}(\text{TlBiTe}_2)_x$ and $(\text{TlBiSe}_2)_{1-x}(\text{TlBiTe}_2)_x$ demonstrate very similar band dispersion, since both systems have broken band alignment and common constituent materials. Replacing TlBiSe_2 with TlBiS_2 does not make a significant change in the band dispersion, although the Se atom has a bigger spin-orbit coupling constant than the S atom. However, the spin texture is changed for the Dirac-like states. At $x = 13/18$ (Figure 4(d)), a 2D character Dirac-like point arises around -0.5 eV and the corresponding charge density is localized at the interface, mostly on the TlBiTe_2 side (Figure 4(g), right). However, the spin texture (Figure 4(d-f), inset) indicates that these bands do not have opposite spin direction for the upper and lower branches. Therefore, they are trivial metallic interface states. In addition, the TlBiS_2 and TlBiTe_2 bands cross each other away from the time reversal invariant momentum (TRIM) points along the \bar{K} - $\bar{\Gamma}$ path direction, and this crossing happens between opposite spin bands (Figure 4(d-f), red circle). Recently, similar bands have been reported for Bi_4Se_3 and Bi_1Te_1 superlattices.^{29,30} In contrast to our findings, their results showed that the band crossing along the \bar{M} - $\bar{\Gamma}$ direction is gapless and mirror symmetry pro-

tected, and also that another band crossing happens at $\bar{\Gamma}$: the state is dually protected.

CONCLUSION

In this work, the electronic properties of thermodynamically formed topological insulator superlattices have been investigated. Our results demonstrate that it is possible to obtain self-assembled interfaces between iso-structural and iso-valent materials with interesting electronic properties. Compositional tuning induces various phenomena, such as topological interface states, spin texture gain by non-topological states, band inversion, band crossing between the TRIM points, and Rashba-like states. The emergence of these phenomena is related to the band alignment and composition of the systems. With this method, we demonstrate that obtaining 2D metallic channels in a 3D insulating matrix is possible for TI superlattices without vacuum interfaces. Since these states are protected from the environment, they can be useful for device applications. These findings suggest that the combination of thermodynamic and electronic properties can create a pathway for investigating thermodynamically driven interfaces to obtain possible novel phenomena, which may help to explore more materials for spintronic devices and further applications.

ACKNOWLEDGMENTS

The authors acknowledge support by DOD-ONR (N00014-13-1-0635, N00014-15-1-2863, N00014-16-1-2326). The consortium AFLOW.org acknowledges Duke University – Center for Materials Genomics – for computational support. S.C. acknowledges the Alexander von Humboldt Foundation for financial support. The authors thank Corey Oses, David Hicks, Eric Gossett, and Ohad Levy for helpful discussions.

SUPPORTING INFORMATION

Optimized lattice parameters and atom resolved band structures of rhombohedral TlBiX_2 ($X=\text{S, Se, Te}$) bulk systems; atom resolved surface electronic structure of X -terminated and Tl-terminated (111) surfaces of TlBiX_2 ($X=\text{S, Se, Te}$).

* stefano@duke.edu

¹ J. D. Cressler and G. Niu, *Silicon-germanium Heterojunction Bipolar Transistors* (Artech House, London, Boston, 2003).

² M. Razeghi and A. Rogalski, *Semiconductor ultraviolet detectors*, J. Appl. Phys. **79**, 7433 (1996).

³ M. Rizzi, M. D'Aloia, and B. Castagnolo, *Semiconductor Detectors and Principles of Radiation-matter Interaction*, J. Appl. Sci. **10**, 3141–3155 (2010).

⁴ D.-K. Hwang, S.-H. Kang, J.-H. Lim, E.-J. Yang, J.-Y. Oh, J.-H. Yang, and S.-J. Park, *p-ZnO/n-GaN heterostructure ZnO light-emitting diodes*, Appl. Phys. Lett. **86**, 222101

- (2005).
- ⁵ R. Köhler, A. Tredicucci, F. Beltram, H. E. Beere, E. H. Linfield, A. G. Davies, D. A. Ritchie, R. C. Iotti, and F. Rossi, *Terahertz semiconductor-heterostructure laser*, *Nature* **417**, 156–159 (2002).
 - ⁶ S. Curtarolo, G. L. W. Hart, M. Buongiorno Nardelli, N. Mingo, S. Sanvito, and O. Levy, *The high-throughput highway to computational materials design*, *Nat. Mater.* **12**, 191–201 (2013).
 - ⁷ G. J. Exarhos and X.-D. Zhou, *Discovery-based design of transparent conducting oxide films*, *Thin Solid Films* **515**, 7025–7052 (2007).
 - ⁸ E. Sachet, C. T. Shelton, J. S. Harris, B. E. Gaddy, D. L. Irving, S. Curtarolo, B. F. Donovan, P. E. Hopkins, P. A. Sharma, A. L. Sharma, J. Ihlefeld, S. Franzen, and J.-P. Maria, *Dysprosium-doped cadmium oxide as a gateway material for mid-infrared plasmonics*, *Nat. Mater.* **14**, 414–420 (2015).
 - ⁹ E. Nakamura and K. Sato, *Managing the scarcity of chemical elements*, *Nat. Mater.* **10**, 158–161 (2011).
 - ¹⁰ D. Usanmaz, P. Nath, J. J. Plata, G. L. W. Hart, I. Takeuchi, M. Buongiorno Nardelli, M. Fornari, and S. Curtarolo, *First principles thermodynamical modeling of the binodal and spinodal curves in lead chalcogenides*, *Phys. Chem. Chem. Phys.* **18**, 5005–5011 (2016).
 - ¹¹ T. Hirahara, G. Bihlmayer, Y. Sakamoto, M. Yamada, H. Miyazaki, S.-I. Kimura, S. Blügel, and S. Hasegawa, *Interfacing 2D and 3D Topological Insulators: Bi(111) Bilayer on Bi₂Te₃*, *Phys. Rev. Lett.* **107**, 166801 (2011).
 - ¹² M. H. Berntsen, O. Götzberg, B. M. Wojek, and O. Tjernberg, *Direct observation of decoupled Dirac states at the interface between topological and normal insulators*, *Phys. Rev. B* **88**, 195132 (2013).
 - ¹³ T. Shoman, A. Takayama, T. Sato, S. Souma, T. Takahashi, T. Oguchi, K. Segawa, and Y. Ando, *Topological proximity effect in a topological insulator hybrid*, *Nat. Commun.* **6**, 6547 (2015).
 - ¹⁴ B. Yan and S.-C. Zhang, *Topological materials*, *Rep. Prog. Phys.* **75**, 096501 (2012).
 - ¹⁵ Y. L. Chen, J. G. Analytis, J.-H. Chu, Z. K. Liu, S.-K. Mo, X. L. Qi, H. J. Zhang, D. H. Lu, X. Dai, Z. Fang, S. C. Zhang, I. R. Fisher, Z. Hussain, and Z.-X. Shen, *Experimental Realization of a Three-Dimensional Topological Insulator, Bi₂Te₃*, *Science* **325**, 178–181 (2009).
 - ¹⁶ H. Zhang, C.-X. Liu, X.-L. Qi, X. Dai, Z. Fang, and S.-C. Zhang, *Topological insulators in Bi₂Se₃, Bi₂Te₃ and Sb₂Te₃ with a single Dirac cone on the surface*, *Nat. Phys.* **5**, 438–442 (2009).
 - ¹⁷ T. Zhang, P. Cheng, X. Chen, J.-F. Jia, X. Ma, K. He, L. Wang, H. Zhang, X. Dai, Z. Fang, X. Xie, and Q.-K. Xue, *Experimental Demonstration of Topological Surface States Protected by Time-Reversal Symmetry*, *Phys. Rev. Lett.* **103**, 266803 (2009).
 - ¹⁸ K. Yang, W. Setyawan, S. Wang, M. Buongiorno Nardelli, and S. Curtarolo, *A search model for topological insulators with high-throughput robustness descriptors*, *Nat. Mater.* **11**, 614–619 (2012).
 - ¹⁹ T. H. Hsieh, H. Lin, J. Liu, W. Duan, A. Bansil, and L. Fu, *Topological crystalline insulators in the SnTe material class*, *Nat. Commun.* **3**, 982 (2012).
 - ²⁰ P. Dziawa, B. J. Kowalski, K. Dybko, R. Buczko, A. Szczerbakow, M. Szot, E. Łusakowska, T. Balasubramanian, B. M. Wojek, M. H. Berntsen, O. Tjernberg, and T. Story, *Topological crystalline insulator states in Pb_{1-x}Sn_xSe*, *Nat. Mater.* **11**, 1023–1027 (2012).
 - ²¹ Y. Tanaka, Z. Ren, T. Sato, K. Nakayama, S. Souma, T. Takahashi, K. Segawa, and Y. Ando, *Experimental realization of a topological crystalline insulator in SnTe*, *Nat. Phys.* **8**, 800–803 (2012).
 - ²² Y. Ando, *Topological insulator materials*, *J. Phys. Soc. Jpn.* **82**, 102001 (2013).
 - ²³ K. Nakayama, K. Eto, Y. Tanaka, T. Sato, S. Souma, T. Takahashi, K. Segawa, and Y. Ando, *Manipulation of Topological States and the Bulk Band Gap Using Natural Heterostructures of a Topological Insulator*, *Phys. Rev. Lett.* **109**, 236804 (2012).
 - ²⁴ T. Rauch, M. Flieger, J. Henk, and I. Mertig, *Nontrivial interface states confined between two topological insulators*, *Phys. Rev. B* **88**, 245120 (2013).
 - ²⁵ G. Wu, H. Chen, Y. Sun, X. Li, P. Cui, C. Franchini, J. Wang, X.-Q. Chen, and Z. Zhang, *Tuning the vertical location of helical surface states in topological insulator heterostructures via dual-proximity effects*, *Sci. Rep.* **3**, 1233 (2013).
 - ²⁶ Z. Chen, L. Zhao, K. Park, T. A. Garcia, M. C. Tamargo, and L. Krusin-Elbaum, *Robust Topological Interface and Charge Transfer in Epitaxial Bi₂Se₃/II-VI Semiconductor Superlattices*, *Nano Lett.* **15**, 6365 (2015).
 - ²⁷ S.-Y. Xu, Y. Xia, L. A. Wray, S. Jia, F. Meier, J. H. Dil, J. Osterwalder, B. Slomski, A. Bansil, H. Lin, R. J. Cava, and M. Z. Hasan, *Topological phase transition and texture inversion in a tunable topological insulator*, *Science* **332**, 560 (2011).
 - ²⁸ Y. Zhang, K. He, C.-Z. Chang, C.-L. Song, L.-L. Wang, X. Chen, J.-F. Jia, Z. Fang, X. Dai, W.-Y. Shan, S.-Q. Shen, Q. Niu, X.-L. Qi, S.-C. Zhang, X.-C. Ma, and Q.-K. Xue, *Crossover of the three-dimensional topological insulator Bi₂Se₃ to the two-dimensional limit*, *Nat. Phys.* **6**, 584–588 (2010).
 - ²⁹ M. et al., *Eschbach, Bi₁Te₁ is a dual topological insulator*, *Nat. Commun.* **8**, 14976 (2017).
 - ³⁰ A. P. Weber, Q. D. Gibson, H. Ji, A. N. Caruso, A. V. Fedorov, R. J. Cava, and T. Valla, *Gapped Surface States in a Strong-Topological-Insulator Material*, *Phys. Rev. Lett.* **114**, 256401 (2015).
 - ³¹ I. Belopolski, S.-Y. Xu, N. Koirala, C. Liu, G. Bian, V. N. Strocov, G. Chang, M. Neupane, N. Alidoust, D. Sanchez, H. Zheng, M. Brahlek, V. Rogalev, T. Kim, N. C. Plumb, C. Chen, F. Bertran, P. Le Fèvre, A. Taleb-Ibrahimi, M.-C. Asensio, M. Shi, H. Lin, M. Hoesch, S. Oh, and M. Z. Hasan, *A novel artificial condensed matter lattice and a new platform for one-dimensional topological phases*, *Sci. Adv.* **3**, e1501692 (2017).
 - ³² J. A. Hagemann, X. Li, S. Chowdhury, S.-N. Dong, S. Rouvimov, S. J. Pookpanratana, K. M. Yu, T. A. Orlova, T. B. Bolin, C. U. Segre, D. G. Seiler, C. A. Richter, X. Liu, M. Dobrowolska, and J. K. Furdyna, *Molecular beam epitaxy growth and structure of self-assembled Bi₂Se₃/Bi₂MnSe₄ multilayer heterostructures*, *New J. Phys.* **19**, 085002 (2017).
 - ³³ A. A. Burkov and L. Balents, *Weyl Semimetal in a Topological Insulator Multilayer*, *Phys. Rev. Lett.* **107**, 127205 (2011).
 - ³⁴ J. Androulakis, C.-H. Lin, H.-J. Kong, C. Uher, C.-I. Wu, T. Hogan, B. A. Cook, T. Caillat, K. M. Paraskevopoulos, and M. G. Kanatzidis, *Spinodal Decomposition and Nucleation and Growth as a Means to Bulk Nanostructured Thermoelectrics: Enhanced Performance in Pb_{1-x}Sn_xTe-PbS*, *J.*

- Amer. Chem. Soc. **129**, 9780–9788 (2007).
- ³⁵ L.-D. Zhao, J. He, S. Hao, C.-I. Wu, T. P. Hogan, C. Wolverton, V. P. Dravid, and M. G. Kanatzidis, *Raising the thermoelectric performance of p-type PbS with endotaxial nanostructuring and valence-band offset engineering using CdS and ZnS*, J. Amer. Chem. Soc. **134**, 16327–16336 (2012).
- ³⁶ Y. Gelbstein, B. Dado, O. Ben-Yehuda, Y. Sadia, Z. Dashevsky, and M. P. Dariel, *High Thermoelectric Figure of Merit and Nanostructuring in Bulk p-type $Ge_x(Sn_yPb_{1-y})_{1-x}Te$ Alloys Following a Spinodal Decomposition Reaction*, Chem. Mater. **22**, 1054–1058 (2010).
- ³⁷ J. R. Sootsman, J. He, V. P. Dravid, C.-P. Li, C. Uher, and M. G. Kanatzidis, *High thermoelectric figure of merit and improved mechanical properties in melt quenched PbTe-Ge and PbTe- $Ge_{1-x}S_{2x}$ eutectic and hypereutectic composites*, J. Appl. Phys. **105**, 083718 (2009).
- ³⁸ M. Hillert, *A solid-solution model for inhomogeneous systems*, Acta Metallurgica **9**, 525–535 (1961).
- ³⁹ J. W. Cahn, *On spinodal decomposition*, Acta Metallurgica **9**, 795–801 (1961).
- ⁴⁰ J. W. Cahn, *On spinodal decomposition in cubic crystals*, Acta Metallurgica **10**, 179–183 (1962).
- ⁴¹ J. Mannhart and D. G. Schlom, *Oxide Interfaces—An Opportunity for Electronics*, Science **327**, 1607–1611 (2010).
- ⁴² K. Yoshimatsu, T. Okabe, H. Kumigashira, S. Okamoto, S. Aizaki, A. Fujimori, and M. Oshima, *Dimensional-Crossover-Driven Metal-Insulator Transition in $SrVO_3$ Ultrathin Films*, Phys. Rev. Lett. **104**, 147601 (2010).
- ⁴³ K. Yoshimatsu, R. Yasuhara, H. Kumigashira, and M. Oshima, *Origin of Metallic States at the Heterointerface between the Band Insulators $LaAlO_3$ and $SrTiO_3$* , Phys. Rev. Lett. **101**, 026802 (2008).
- ⁴⁴ J. G. Analytis, J.-H. Chu, Y. Chen, F. Corredor, R. D. McDonald, Z. X. Shen, and I. R. Fisher, *Bulk Fermi surface coexistence with Dirac surface state in Bi_2Se_3 : A comparison of photoemission and Shubnikov-de Haas measurements*, Phys. Rev. B **81**, 205407 (2010).
- ⁴⁵ K. Eto, Z. Ren, A. A. Taskin, K. Segawa, and Y. Ando, *Angular-dependent oscillations of the magnetoresistance in Bi_2Se_3 due to the three-dimensional bulk Fermi surface*, Phys. Rev. B **81**, 195309 (2010).
- ⁴⁶ N. P. Butch, K. Kirshenbaum, P. Syers, A. B. Sushkov, G. S. Jenkins, H. D. Drew, and J. Paglione, *Strong surface scattering in ultrahigh-mobility Bi_2Se_3 topological insulator crystals*, Phys. Rev. B **81**, 241301(R) (2010).
- ⁴⁷ B. Yan, C.-X. Liu, H.-J. Zhang, C.-Y. Yam, X.-L. Qi, T. Frauenheim, and S.-C. Zhang, *Theoretical prediction of topological insulators in thallium-based III-V-VI₂ ternary chalcogenides*, EPL-Europhys. Lett. **90**, 37002 (2010).
- ⁴⁸ Q. Zhang, Y. Cheng, and U. Schwingenschlögl, *Emergence of topological and topological crystalline phases in $TlBiS_2$ and $TlSbS_2$* , Sci. Rep. **5**, 8379 (2015).
- ⁴⁹ B. Singh, H. Lin, R. Prasad, and A. Bansil, *Topological phase transition and quantum spin Hall state in $TlBiS_2$* , J. Appl. Phys. **116**, 033704 (2014).
- ⁵⁰ T. Sato, K. Segawa, K. Kosaka, S. Souma, K. Nakayama, K. Eto, T. Minami, Y. Ando, and T. Takahashi, *Unexpected mass acquisition of Dirac fermions at the quantum phase transition of a topological insulator*, Nat. Phys. **7**, 840–844 (2011).
- ⁵¹ S. Souma, M. Komatsu, M. Nomura, T. Sato, A. Takayama, T. Takahashi, K. Eto, K. Segawa, and Y. Ando, *Spin Polarization of Gapped Dirac Surface States Near the Topological Phase Transition in $TlBi(S_{1-x}Se_x)_2$* , Phys. Rev. Lett. **109**, 186804 (2012).
- ⁵² B. Singh, A. Sharma, H. Lin, M. Z. Hasan, R. Prasad, and A. Bansil, *Topological electronic structure and Weyl semimetal in the $TlBiSe_2$ class of semiconductors*, Phys. Rev. B **86**, 115208 (2012).
- ⁵³ A. van de Walle, M. D. Asta, and G. Ceder, *The alloy theoretic automated toolkit: A user guide*, Calphad **26**, 539–553 (2002).
- ⁵⁴ A. van de Walle and G. Ceder, *Automating First-Principles Phase Diagram Calculations*, J. Phase Equilib. **23**, 348–359 (2002).
- ⁵⁵ A. van de Walle and M. D. Asta, *Self-driven lattice-model Monte Carlo simulations of alloy thermodynamic properties and phase diagrams*, Model. Simul. Mater. Sci. Eng. **10**, 521 (2002).
- ⁵⁶ S. Curtarolo, W. Setyawan, G. L. W. Hart, M. Jahnátek, R. V. Chepulskii, R. H. Taylor, S. Wang, J. Xue, K. Yang, O. Levy, M. J. Mehl, H. T. Stokes, D. O. Demchenko, and D. Morgan, *AFLow: An automatic framework for high-throughput materials discovery*, Comput. Mater. Sci. **58**, 218–226 (2012).
- ⁵⁷ K. Yang, C. Oses, and S. Curtarolo, *Modeling Off-Stoichiometry Materials with a High-Throughput Ab-Initio Approach*, Chem. Mater. **28**, 6484–6492 (2016).
- ⁵⁸ C. E. Calderon, J. J. Plata, C. Toher, C. Oses, O. Levy, M. Fornari, A. Natan, M. J. Mehl, G. L. W. Hart, M. Buongiorno Nardelli, and S. Curtarolo, *The AFLow standard for high-throughput materials science calculations*, Comput. Mater. Sci. **108 Part A**, 233–238 (2015).
- ⁵⁹ O. Levy, M. Jahnátek, R. V. Chepulskii, G. L. W. Hart, and S. Curtarolo, *Ordered Structures in Rhenium Binary Alloys from First-Principles Calculations*, J. Amer. Chem. Soc. **133**, 158–163 (2011).
- ⁶⁰ O. Levy, G. L. W. Hart, and S. Curtarolo, *Structure maps for hcp metals from first-principles calculations*, Phys. Rev. B **81**, 174106 (2010).
- ⁶¹ W. Setyawan and S. Curtarolo, *High-throughput electronic band structure calculations: Challenges and tools*, Comput. Mater. Sci. **49**, 299–312 (2010).
- ⁶² O. Levy, G. L. W. Hart, and S. Curtarolo, *Uncovering Compounds by Synergy of Cluster Expansion and High-Throughput Methods*, J. Amer. Chem. Soc. **132**, 4830–4833 (2010).
- ⁶³ G. L. W. Hart, S. Curtarolo, T. B. Massalski, and O. Levy, *Comprehensive Search for New Phases and Compounds in Binary Alloy Systems Based on Platinum-Group Metals, Using a Computational First-Principles Approach*, Phys. Rev. X **3**, 041035 (2013).
- ⁶⁴ A. R. Supka, T. E. Lyons, L. S. I. Liyanage, P. D’Amico, R. Al Rahal Al Orabi, S. Mahatara, P. Gopal, C. Toher, D. Ceresoli, A. Calzolari, S. Curtarolo, M. Buongiorno Nardelli, and M. Fornari, *AFLow π : A minimalist approach to high-throughput ab initio calculations including the generation of tight-binding hamiltonians*, Comput. Mater. Sci. **136**, 76–84 (2017).
- ⁶⁵ M. J. Mehl, D. Hicks, C. Toher, O. Levy, R. M. Hanson, G. L. W. Hart, and S. Curtarolo, *The AFLow Library of Crystallographic Prototypes: Part 1*, Comput. Mater. Sci. **136**, S1–S828 (2017).
- ⁶⁶ S. Curtarolo, W. Setyawan, S. Wang, J. Xue, K. Yang, R. H. Taylor, L. J. Nelson, G. L. W. Hart, S. Sanvito, M. Buongiorno Nardelli, N. Mingo, and O. Levy, *AFLowLIB.ORG: A distributed materials properties repository from high-*

- throughput *ab initio* calculations, *Comput. Mater. Sci.* **58**, 227–235 (2012).
- ⁶⁷ R. H. Taylor, F. Rose, C. Toher, O. Levy, K. Yang, M. Buongiorno Nardelli, and S. Curtarolo, *A RESTful API for exchanging materials data in the AFLOWLIB.org consortium*, *Comput. Mater. Sci.* **93**, 178–192 (2014).
- ⁶⁸ F. Rose, C. Toher, E. Gossett, C. Oses, M. Buongiorno Nardelli, M. Fornari, and S. Curtarolo, *AFLUX: The LUX materials search API for the AFLOW data repositories*, *Comput. Mater. Sci.* **137**, 362–370 (2017).
- ⁶⁹ G. Kresse and J. Hafner, *Ab initio molecular dynamics for liquid metals*, *Phys. Rev. B* **47**, 558–561 (1993).
- ⁷⁰ P. E. Blöchl, *Projector augmented-wave method*, *Phys. Rev. B* **50**, 17953–17979 (1994).
- ⁷¹ J. P. Perdew, K. Burke, and M. Ernzerhof, *Generalized Gradient Approximation Made Simple*, *Phys. Rev. Lett.* **77**, 3865–3868 (1996).
- ⁷² Y. I. Jafarov, S. Z. Imamaliev, V. P. Zlomanov, and M. B. Babanly, *Phase equilibria in the reciprocal system $3Tl_2S + Bi_2Te_3 \leftrightarrow 3Tl_2Te + Bi_2S_3$* , *Inorg. Mater.* **50**, 551–558 (2014).
- ⁷³ M. B. Babanly, Y. I. Jafarov, Z. S. Aliev, and I. R. Amirasanov, *Chemistry of Thallium-based Topological Insulators*, *ACSJ* **10**(1), 1–13 (2016).
- ⁷⁴ A. H. Cottrell, *An introduction to metallurgy* (St. Martin's Press, UK, 1967).
- ⁷⁵ B. P. Burton, A. van de Walle, and U. Kattner, *First-principles phase diagram calculations for the wurtzite-structure systems AlN-GaN, GaN-InN, and AlN-InN*, *J. Appl. Phys.* **100**, 113528 (2006).
- ⁷⁶ O. Adjaoud, G. Steinle-Neumann, B. P. Burton, and A. van de Walle, *First-principles phase diagram calculations for the HfC-TiC, ZrC-TiC, and HfC-ZrC solid solutions*, *Phys. Rev. B* **80**, 134112 (2009).
- ⁷⁷ Z. T. Y. Liu, B. P. Burton, S. V. Khare, and P. Sarin, *First-principles phase diagram calculations for the carbonate quaternary systems $CaCO_3$ - $ZnCO_3$, $CdCO_3$ - $ZnCO_3$, $CaCO_3$ - $CdCO_3$ and $MgCO_3$ - $ZnCO_3$* , *Chem. Geol.* **443**, 137–145 (2016).
- ⁷⁸ T. Kanai, T. Sawada, J. Yamanaka, and K. Kitamura, *Equilibrium Characteristic at Ordered-Disordered Phase Boundary in Centrifuged Nonequilibrium Colloidal-Crystal System*, *J. Amer. Chem. Soc.* **126**, 13210–13211 (2004).
- ⁷⁹ J. de la Figuera, F. Léonard, N. C. Bartelt, R. Stumpf, and K. F. McCarty, *Nanoscale Periodicity in Stripe-Forming Systems at High Temperature: Au/W(110)*, *Phys. Rev. Lett.* **100**, 186102 (2008).
- ⁸⁰ J. Chang, L. F. Register, S. K. Banerjee, and B. Sahu, *Density functional study of ternary topological insulator thin films*, *Phys. Rev. B* **83**, 235108 (2011).
- ⁸¹ T. P. Pearsall, ed., *Strained-Layer Superlattices:Physics*, vol. 32 (Academic Press, New York, 1990).
- ⁸² T. P. Pearsall, ed., *Strained-Layer Superlattices:Materials Science and Technology*, vol. 33 (Academic Press, New York, 1991).
- ⁸³ K. Kuroda, M. Ye, A. Kimura, S. V. Eremeev, E. E. Krasovskii, E. V. Chulkov, Y. Ueda, K. Miyamoto, T. Okuda, K. Shimada, H. Namatame, and M. Taniguchi, *Experimental Realization of a Three-Dimensional Topological Insulator Phase in Ternary Chalcogenide $TlBiSe_2$* , *Phys. Rev. Lett.* **105**, 146801 (2010).
- ⁸⁴ S. V. Eremeev, Y. M. Koroteev, and E. V. Chulkov, *Ternary Thallium-Based Semimetal Chalcogenides $Tl-V-VI_2$ as a New Class of Three-Dimensional Topological Insulators*, *JETP Lett.* **91**, 594 (2010).
- ⁸⁵ S. V. Eremeev, G. Bihlmayer, M. Vergniory, Y. M. Koroteev, T. V. Menshchikova, J. Henk, A. Ernst, and E. V. Chulkov, *Ab initio electronic structure of thallium-based topological insulators*, *Phys. Rev. B* **83**, 205129 (2011).
- ⁸⁶ Q. Zhang, Z. Zhang, Y. Zhu, U. Schwingenschlögl, and Y. Cui, *Exotic Topological Insulator States and Topological Phase Transition in Sb_2Se_3 - Bi_2Se_3 Heterostructures*, *ACS Nano* **6**, 2345 (2012).
- ⁸⁷ K.-H. Jin, H. W. Yeom, and S.-H. Jhi, *Band structure engineering of topological insulator heterojunctions*, *Phys. Rev. B* **93**, 075308 (2016).
- ⁸⁸ J. A. Hutasoit and T. D. Stanescu, *Induced spin texture in semiconductor/topological insulator heterostructures*, *Phys. Rev. B* **84**, 085103 (2011).
- ⁸⁹ L. Seixas, D. West, A. Fazzio, and S. B. Zhang, *Vertical twinning of the Dirac cone at the interface between topological insulators and semiconductors*, *Nat. Commun.* **6**, 7630 (2015).
- ⁹⁰ R. Takahashi and S. Murakami, *Gapless Interface States between Topological Insulators with Opposite Dirac Velocities*, *Phys. Rev. Lett.* **107**, 166805 (2011).
- ⁹¹ C. De Beule and B. Partoens, *Gapless interface states at the junction between two topological insulators*, *Phys. Rev. B* **87**, 115113 (2013).
- ⁹² J. C. Johannsen, G. Autés, A. Crepaldi, S. Moser, B. Casarin, F. Cilento, M. Zacchigna, H. Berger, A. Margrez, P. Bugnon, J. Avila, M. C. Asensio, F. Parmigiani, O. V. Yazyev, and M. Grioni, *Engineering the topological surface states in the $(Sb_2)_m$ - Sb_2Te_3 ($m=0-3$) superlattice series*, *Phys. Rev. B* **91**, 201101(R) (2015).
- ⁹³ Q. D. Gibson, L. M. Schoop, A. P. Weber, H. Ji, S. Nadj-Perge, I. K. Drozdov, H. Beidenkopf, J. T. Sadowski, A. Fedorov, A. Yazdani, T. Valla, and R. J. Cava, *Termination-dependent topological surface states of the natural superlattice phase Bi_4Se_3* , *Phys. Rev. B* **88**, 081108(R) (2013).